ELSEVIER

Ultramicroscopy 69 (1997) 69–81

ultramicroscopy

Theory of the cross sections for inelastic scattering of electrons by core level excitations in solids

D.R. Penn[a,*], C.W. Clark[a], C.J. Powell[a], T. Fulop[b], S. Tanuma[c]

[a] *National Institute of Standards and Technology, Gaithersburg, MD 20899, USA*
[b] *Chalmers University of Technology, School of Electrical Engineering, S-412 96 Gothenburg, Sweden*
[c] *Japan Energy ARC Co. Ltd., 3-17-35 Niizo-Minami, Toda, Saitama 335, Japan*

Received 15 November 1995; received in revised form 7 April 1997

Abstract

A calculation of cross sections for the inelastic scattering of electrons from core levels is carried out based on a model in which core level electrons are excited into a free-electron-like band state. A simplified model is also developed that assumes oscillator strengths appropriate to band-to-band excitations in solids. The results for Al L_{23} and Mo M_{45} cross sections are compared with a number of previous calculations. These previous calculations include: (a) the constant-oscillator-strength model, (b) the Rez model (based on excitations to atomic-like states), and (c) the semi-empirical hydrogenic model proposed by Egerton. We have incorporated optical data into all of the models considered in this paper with the exception of Egerton's. Calculations are presented for incident electron energies of 100, 200 and 500 keV, collection angles of 1–41 mrad, and energy collection windows of 20–200 eV. Comparison is also made with experiment where possible and reasonable agreement is found.

1. Introduction

A discussion of the factors affecting the accuracy of elemental analysis by electron energy-loss spectroscopy has been given by Egerton [1]. A key ingredient is knowledge of the inelastic scattering cross sections for excitations from the core levels in solids. Previous theoretical calculations have been based on either hydrogenic atomic models [2–8] or on numerical Hartree–Slater type calculations for atoms [9–14]. Calculations by Egerton [7] and Luo and Zeitler [8] make use of experimental optical data to calculate cross sections for some elements.

This paper presents a new model for the calculation of innershell excitation cross sections in which the final state of the excited electron is described by a free-electron band rather than the excited state of an atom. Experimental optical data are incorporated into the model in such a way that energy losses involving small momentum transfers are taken into account in a correct manner, i.e. the

* Corresponding author.

PII S0304-3991(97)00039-9

calculated cross sections are expected to be correct for small-angle scattering. The availability of optical data should make it possible to apply this model to a number of solids.

A simplified alternative method for calculating cross sections is also developed, based on previous work appropriate to band-to-band transitions in solids. This method is much more convenient to use, but has no a priori justification. It gives numerical results that are similar to those of the first method for a limited range of parameters.

The theory for the cross section calculation is presented in Section 2 and the simplified method is described in Section 3. Cross sections for the excitations of Al L_{23} and Mo M_{45} core electrons based on the method of Sections 2 and 3 are given as examples of our proceedure in Section 4. Cross sections predicted by our model are presented for incident electron energies of 100, 200 and 500 keV, collection angles of 1–41 mrad, and energy collection windows of 20–200 eV. We also compare our calculated cross sections to those calculated using alternative models. These models include: (a) our simplified model, (b) the constant-oscillator-strength model, (c) the Rez model (based on atomic cross sections), (d) the semi-empirical atomic model introduced by Egerton with cross sections determined from Egerton's SIGMAL3 [7] program for Al. The calculations are compared for incident electron energies of 100 keV, collection angles of 1–41 mrad, and energy collection windows of 20–200 eV. A cross section calculation for a single set of parameters has been given in Ref. [8] for various atoms, and we compare our result for Mo M_{45} excitations with the value from that reference. Cross sections calculated with the present model have been compared with experimental results [19–21] for Al L_{23} excitations and the results are in reasonable agreement. Section 5 gives the conclusions of this work.

2. Theory of the cross sections

The differential cross section for inelastic scattering of an electron from a target is

$$\frac{d^2\sigma}{d\Omega\, dE} = \frac{4\gamma^2 R}{E^2 q^2}\frac{k_1}{k_0}\frac{df(\boldsymbol{q},E)}{dE} \tag{1a}$$

involving energy loss E and momentum transfer q into a solid angle Ω is given by

$$\gamma = (1 - v^2/c^2)^{1/2}, \tag{1b}$$

where v is the velocity of the incident electron and c is the speed of light. The quantity $R = 13.6$ eV, k_0, k_1 are the momenta of the electrons before and after scattering, and df/dE is the generalized differential oscillator strength of the target. For incident electrons of energy E_0 much greater than the energy loss, the momenta satisfy $k_1 \sim k_0$. Use of $d\Omega = \pi d(q^2)/k_1 k_0$ in Eq. (1a) gives

$$\frac{d\sigma}{dE} = \frac{4\pi}{E}\frac{\gamma^2}{\gamma^2 - 1} R \frac{\hbar^2}{m^2c^2}\int \frac{d(q^2)}{q^2}\frac{df(q,E)}{dE} \tag{2}$$

where m is the electron mass and where the relationship

$$k_0^2 = (m^2c^2/\hbar^2)(\gamma^2 - 1) \tag{3}$$

has been used.

The generalized oscillator strength per atom in a solid is related to the dielectric function, $\epsilon(\boldsymbol{q},\omega)$, by [15]

$$\frac{df}{dE}(\boldsymbol{q},E) = \frac{2E}{\pi E_a^2}\,\mathrm{Im}(-1/\epsilon(\boldsymbol{q},\omega)), \tag{4a}$$

where $\omega = E/\hbar$, E_a is the plasmon energy corresponding to one electron per atom,

$$E_a = \hbar\left(4\pi\frac{N_a}{V}\frac{e^2}{m}\right)^{1/2}, \tag{4b}$$

N_a is the number of atoms, and V is the volume of the solid. For the case of energy loss from core excitations, $\epsilon_1 \sim 1$ and $\epsilon_2 \ll 1$ where ϵ_1, ϵ_2 are the real and imaginary parts of $\epsilon(\boldsymbol{q},\omega)$. Thus,

$$\mathrm{Im}(-1/\epsilon(\boldsymbol{q},\omega)) \approx \epsilon_2(\boldsymbol{q},\omega) \tag{5}$$

and Eqs. (2), (4a), (4b) and (5) give

$$\frac{d\sigma}{dE} = \frac{2}{\pi mc^2}\frac{\gamma^2}{\gamma^2 - 1}\frac{1}{(N_a/V)}\frac{1}{a_0}\int\frac{dq}{q}\epsilon_2(\boldsymbol{q},\omega), \tag{6}$$

where a_0 is the Bohr radius.

The contribution to the imaginary part of the dielectric function of the solid due to excitations

from a given core level described by quantum numbers $c = (n,l,m)$, is given by

$$\epsilon_2^{nl}(\boldsymbol{q},\omega) = \frac{4\pi^2 e^2}{q^2 V} \sum_{m,k} (1 - f_k) \, |\langle k|e^{-i\boldsymbol{q}\cdot\boldsymbol{r}}|c\rangle|^2 \times \delta(E_k - E_c - \hbar\omega), \tag{7}$$

where the summation is over the azimuthal quantum number, m, and the valence band states, k, and f_k is the occupation number of the state k. The corresponding wave functions are $|c\rangle$ and $|k\rangle$, and the energies are E_c and E_k. The valence band of the solid is approximated by a single free-electron-like band with a wave function given by an orthogonalized plane wave

$$|k\rangle = \frac{e^{i\boldsymbol{k}\cdot\boldsymbol{r}}}{V^{1/2}} - \sum_{c'} \left\langle \phi_{c'} \middle| \frac{e^{i\boldsymbol{k}\cdot\boldsymbol{r}}}{V^{1/2}} \right\rangle \phi_{c'}(\boldsymbol{r}), \tag{8}$$

where the summation is over all core states of the atom including the state from which an electron is excited, c. The simplicity of the model for the excited states is compensated for by making use of experimental optical data for the imaginary part of the dielectric function, $\epsilon_2^{EXP}(\omega)$. This is done by multiplying the expression for ϵ_2^{nl} by the factor $r^{nl}(\omega)$,

$$r^{nl}(\omega) = \epsilon_2^{EXP}(\omega)/\epsilon_2^{nl}(q = 0,\omega), \tag{9}$$

where $\epsilon_2^{nl}(q = 0,\omega)$ is the $q = 0$ limit of the calculated dielectric function for the solid, Eq. (7). This procedure ensures that for $q = 0$ the calculated value for ϵ_2^{nl} will agree with the experimental value. Consequently, it is the momentum dependence of $\epsilon_2^{nl}(q,\omega)$ that is modeled here, not the ω dependence.

The summation over k in Eq. (7) requires the evaluation of

$$|M_c(\boldsymbol{k},\boldsymbol{q})|^2 \equiv |\langle k|e^{-i\boldsymbol{q}\cdot\boldsymbol{r}}|c\rangle|^2, \tag{10}$$

where $|k\rangle$ is given by Eq. (8). From Eq. (7), the magnitude of $\boldsymbol{k}$ is given by $E_k = E_c - \hbar\omega$ where $E_k = (\hbar^2/2m)k^2$.

The contribution to the imaginary part of the dielectric function for excitations from the core level n, l is obtained from Eqs. (7) and (9) as

$$\epsilon_2^{nl}(q,\omega) = \frac{ka_0}{\pi} \frac{N_a}{(qa_0)^2} |m_{nl}(k,q)|^2 r^{nl}(\omega), \tag{11}$$

where

$$|m_{nl}(k,q)|^2 = \int d\hat{\Omega}_k \sum_m |M_{nlm}(\boldsymbol{k},\boldsymbol{q})|^2, \tag{12}$$

$\int d\hat{\Omega}_k$ denotes an integration over solid angle, M is given by Eq. (10), k is related to the energy loss $E = \hbar\omega$ by

$$E = (\hbar^2/2m)k^2 - E_v^{nl} \tag{13}$$

and E_v^{nl} is the energy distance from the core level to the bottom of the valence band. Note that the contribution of each atom in the target to $\epsilon_2^{nl}(q,\omega)$ is included (incoherently) through the term N_a in Eq. (11). The cross section per unit energy per atom, $d\sigma^{nl}/dE$, is obtained from Eq. (6).

The experimental quantity of interest is the measured area under an energy loss peak, i.e. the number of electrons collected with energies ranging from threshold, E_t^{nl} to an energy Δ above threshold and covering an angular range from 0 to β where β is the maximum collection angle. The range of integration over q in Eqs. (2) and (6) is related to β. Use of Eq. (11) in Eq. (6) gives

$$\sigma_{nl} = \frac{2}{\pi^2 mc^2} \frac{\gamma^2}{\gamma^2 - 1} \frac{V}{a_0} \int_{E_t^{nl}}^{E_t^{nl}+\Delta} dE \, r^{nl}(E) k a_0 \times \int_{q_{min}}^{q_{max}} \frac{dq}{q} \frac{|m_{nl}(k,q)|^2}{(qa_0)^2}, \tag{14}$$

where γ is given by Eq. (1b), $r^{nl}(E)$ is given by Eq. (9), k is given by Eq. (13), and $|m_{nl}(k,q)|^2$ is defined in Eq. (12). The limit q_{min}, is given by

$$(q_{min}a_0)^2 = E^2/4RT, \tag{15a}$$

where $R = 13.6$ eV and $T = (1/2)\, mv^2$ is the nonrelativistic kinetic energy of the incident electrons that is related to the actual energy E_0 by

$$T = E_0(1 + E_0/2mc^2)/(1 + E_0/mc^2)^2 \tag{15b}$$

The limit q_{max} is defined by

$$(q_{max}a_0)^2 = (q_{min}a_0)^2 + 4\gamma^2(T/R)\sin^2(\beta/2), \tag{15c}$$

where

$$\gamma^2 T = E_0(1 + E_0/2mc^2) \tag{15d}$$

There are additional relativistic corrections [7]; in Eq. (14) for σ_{nl}, the quantity $1/q^2$ is replaced by

$$1/q^2 \to Ra_0^2 C_1 C_2 \tag{16a}$$

where

$$C_1 = Q^{-2} - (2\gamma - 1)[\gamma^2 Q(E_0 - Q)]^{-1} + (E_0 - Q)^{-2} + (E_0 + mc^2)^{-2} \tag{16b}$$

$$C_2 = Q - E_0^2(2\gamma^2 mc^2)^{-1} \tag{16c}$$

and

$$Q = R(qa_0)^2 - (E_0^2/2mc^2) \tag{16d}$$

The quantity $|m_{nl}(k,q)|^2$ given by Eq. (12) appears in the final expression, Eq. (14), for σ_{nl} and is evaluated as follows:

$$|m_{nl}(k,q)|^2 = \int d\hat{\Omega}_k \sum_m \left| \left\langle \frac{e^{i\boldsymbol{k}\cdot\boldsymbol{r}}}{V^{1/2}} - \sum_{n'l'm'} b_{n'l'm'}(\boldsymbol{k}) \phi_{n'l'm'}(\boldsymbol{r}) | e^{-i\boldsymbol{q}\cdot\boldsymbol{r}} | \phi_{nlm}(\boldsymbol{r}) \right\rangle \right|^2 \tag{17a}$$

where

$$b_{n'l'm'}(\boldsymbol{k}) = \left\langle \phi_{n'l'm'} \left| \frac{e^{i\boldsymbol{k}\cdot\boldsymbol{r}}}{V^{1/2}} \right\rangle \right. \tag{17b}$$

and where the summation over $n'l'm'$ includes all core levels. It is shown in Appendix A that if φ_{nlm} is of the form

$$\phi_{nlm}(\boldsymbol{r}) = R_{nl}(r) Y_{lm}(\hat{\Omega}_r), \tag{18}$$

then

$$|m_{nl}(k,q)|^2 = \frac{(4\pi)^2}{V} \sum_{l'l''} (2l+1)(2l''+1)(2'+1) \begin{pmatrix} l' & l'' & l \\ 0 & 0 & 0 \end{pmatrix} \times \left\{ \sum_{n'n''} u_{n'l'}(k) u_{n''l'}(k) \theta_{nn'll'l'}(q) \theta_{nn''ll'l'}(q) - 2 \sum_{n'} u_{n'l'}(k) \theta_{nn'll'l'}(q) \Gamma_{nll'l'}(k,q) \right\} + \frac{(4\pi)^2}{V} \int (2l+1) u_{nl}(|\boldsymbol{k}+\boldsymbol{q}|)^2 \, d\Omega_k, \tag{19a}$$

where

$$u_{nl}(k) = \int_0^\infty r^2 \, dr R_{nl}(r) j_l(kr) \tag{19b}$$

$$\theta_{nn'll'l'}(q) = \int_0^\infty r^2 \, dr R_{nl}(r) R_{n'l'}(r) j_{l'}(qr) \tag{19c}$$

and

$$\Gamma_{nll'l'}(k,q) = \int_0^\infty r^2 dr R_{nl}(r) j_{l'}(kr) j_{l'}(qr) \tag{19d}$$

and $\begin{pmatrix} l' & l'' & l \\ 0 & 0 & 0 \end{pmatrix}$ is a 3-j symbol and $j_l(kr)$ is a spherical Bessel function.

It is shown in Appendix B that for $q \to 0$

$$|m_{nl}(k, q \to 0)|^2 = \frac{(4\pi)^2}{V} q^2 \times \left[\frac{1}{3}(l+1) \frac{(2l+1)}{(2l+3)} A_{l+1,nl}^2 + \frac{1}{3} l A_{l-1,nl}^2 \right], \tag{20a}$$

where

$$A_{l_1,nl} = \int_0^\infty r^3 \, dr j_{l_1}(kr) R_{nl}(r) - \sum_{n_1} \int_0^\infty r^2 \, dr j_{l_1}(kr) \times R_{n_1 l_1}(r) \int_0^\infty r^3 \, dr R_{n_1 l_1}(r) R_{nl}(r), \tag{20b}$$

where $l_1 = l \pm 1$.

In order to evaluate $|m_{nl}(k,q)|^2$ numerically the atomic wave functions $R_{nl}(r) Y_{lm}(\hat{\Omega}_r)$ are obtained from tables [16] of Roothan Hartree–Fock atomic wave functions and $R_{nl}(r)$ takes the form of a sum of powers of r times exponential functions of r, i.e., $r^p e^{-\xi r}$ where p is an integer. This procedure allows most of the integrations appearing in Eqs. (19a), (19b), (19c), (19d), (20a) and (20b) to be done analytically.

3. Alternative method for calculation of the cross section

A useful method for calculating the inelastic mean free path of a fast electron in a solid due to scattering by conduction electrons was suggested by Penn [17]. This method is the basis for a general scheme developed by Tanuma et al. [18] in which

inelastic mean free paths are predicted from a Bethe-like formula using parameters of the solid such as density, number of valence electrons per atom, the band-gap energy, and the atomic or molecular weight.

The method developed by Penn gives an approximate expression for the dielectric function of a solid. It is based on a type of statistical approximation in which the solid is characterized by the Lindhard dielectric function. The Lindhard function describes the response of a free-electron gas to an excitation and depends on the electron density of the solid. In this version of the statistical approximation, the dielectric function is averaged over the electron density of the solid in such a way that the predicted value of $\mathrm{Im}(1/\epsilon(q=0,\omega))$ is equal to the measured optical value, $\mathrm{Im}(-1/\epsilon^{\mathrm{EXP}}(\omega))$. The formula for $\mathrm{Im}(-1/\epsilon(q,\omega))$ is

$$\mathrm{Im}\frac{-1}{\epsilon(q,\omega)} = \int_0^\infty \mathrm{d}\omega_p G(\omega_p)\mathrm{Im}\frac{-1}{\epsilon_L(q,\omega;\omega_p)} \tag{21a}$$

where

$$G(\omega) = \frac{2}{\pi\omega}\mathrm{Im}\frac{-1}{\epsilon^{\mathrm{EXP}}(\omega)}, \tag{21b}$$

and $\epsilon_L(q,\omega;\omega_p)$ is the Lindhard dielectric function at a value of the electron density n such that

$$\omega_p^2 = \frac{4\pi n e^2}{m}. \tag{21c}$$

For electron energies much greater than the plasmon energy, the Lindhard dielectric function can be replaced by a one pole approximation

$$\mathrm{Im}\frac{-1}{\epsilon(q,\omega;\omega_p)} = \frac{\pi}{2}\frac{\omega_p^2}{\omega_p(q)}\delta(\omega-\omega_p(q)), \tag{22a}$$

where

$$\omega_p^2(q) = \omega_p^2 + \tfrac{1}{3}[v_F(\omega_p)q]^2 + (\hbar q^2/2m)^2, \tag{22b}$$

where $v_F(\omega_p)$ is the Fermi velocity evaluated for a free electron gas with a plasmon energy ω_p. A simpler version of the one-pole approximation is

$$\omega_p(q) = \omega_p + \frac{\hbar^2 q^2}{2m}. \tag{22c}$$

This method of approximating $\mathrm{Im}(-1/\epsilon(q,\omega))$ is primarily a scheme for estimating the q dependence since the ω dependence is fixed by the condition $\mathrm{Im}(-1/\epsilon(q=0,\omega)) = \mathrm{Im}(-1/\epsilon^{\mathrm{EXP}}(\omega))$. Because of the simplicity of this method relative to that described in the previous section, it will now be applied to the problem of electron scattering from core states even though there is no a priori reason why it should give accurate results. Eq. (22c) is used in Eq. (22a) to obtain

$$\mathrm{Im}\frac{-1}{\epsilon(q,\omega)} = \frac{(\omega-(\hbar q^2/2m))}{\omega}\mathrm{Im}\left(\frac{-1}{\epsilon^{\mathrm{EXP}}(\omega-(\hbar q^2/2m))}\right). \tag{23}$$

The innershell excitation cross section is obtained from Eqs. (2), (4a) and (23). The relativistic corrections given by Eqs. (16a), (16b), (16c) and (16d) are also used.

In the next section the numerical results obtained from this method will be compared with those described in Section 2.

4. Numerical results

The formalism presented in Section 2 is applied to the case of Al L_{23} excitations ($n=2$, $l=1$) and Mo M_{45} excitations ($n=3$, $l=2$) for which there are good optical data available for $\epsilon_2^{\mathrm{EXP}}(\omega)$ [19]. Calculated cross sections for the incident electron energy $E_0 = 100$ keV are shown in Figs. 1 and 2 for values for the collection angle ranging from $\beta = 1$–41 mrad, and for values of the energy window, Δ, from 20 to 200 eV. The very different behavior seen in the two figures is due to the differences in the core level wave functions for the p state of Al and the d state of Mo. This sensitivity to the core state strongly effects the q dependence of the matrix element in Eq. (7). Tables 1 and 2 give numerical values of the cross sections for Al and Mo, respectively. Results are reported for incident electron energies of 100, 200 and 500 keV, collection angles β from 1–41 mrad, and energy windows Δ from 20–200 eV.

The simplified method for calculating the cross section presented in Section 3 is now compared with the more fundamental approach of Section 2 for the cases of Al L_{23} and Mo M_{45} excitations. The

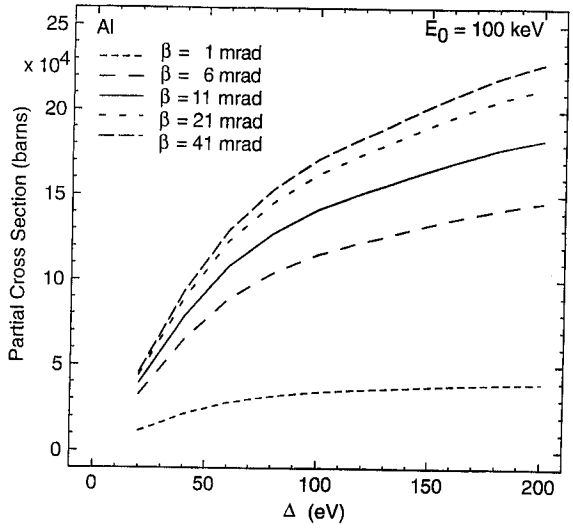

Fig. 1. Calculations of the cross section versus energy collection window Δ predicted by our model for Al L_{23} excitations. The incident electron energy is 100 keV. Values of the collection angle β vary from 1 to 41 mrad.

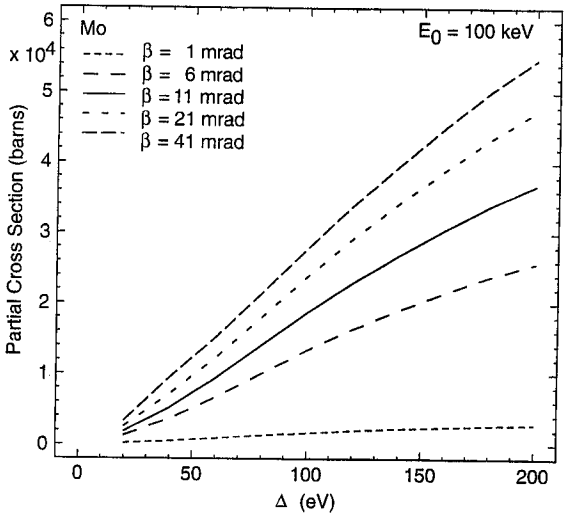

Fig. 2. Same as Fig. 1, but for Mo M_{45} excitations.

cross sections determined in Section 2 will be denoted by σ and those from Section 3 by σ_A. The percentage difference $100(\sigma - \sigma_A)/\sigma$ versus Δ is shown in Figs. 3 and 4 for Al and Mo, respectively, for an incident electron energy of 100 keV and

Table 1
Values of the Al L_{23} cross sections given by our calculations

β (mrad)	Δ (eV)	$E_0 = 100$ keV σ (barns)	$E_0 = 200$ keV σ (barns)	$E_0 = 500$ keV σ (barns)
1	20	1.15×10^4	1.21×10^4	1.29×10^4
	40	2.15	2.33	2.55
	60	2.81	3.11	3.48
	80	3.18	3.59	4.07
	100	3.43	3.93	4.51
	120	3.58	4.14	4.81
	140	3.71	4.33	5.08
	160	3.81	4.49	5.32
	180	3.89	4.62	5.53
	200	3.95	4.72	5.69
6	20	3.27	2.54	2.08
	40	6.49	5.08	4.21
	60	8.86	6.99	5.82
	80	10.40	8.24	6.90
	100	11.53	9.18	7.73
	120	12.31	9.84	8.31
	140	13.00	10.44	8.85
	160	13.63	10.99	9.36
	180	14.19	11.48	9.82
	200	14.61	11.86	10.17
11	20	3.92	2.87	2.20
	40	7.85	5.80	4.48
	60	10.79	8.01	6.23
	80	12.72	9.49	7.39
	100	14.17	10.60	8.29
	120	15.18	11.39	8.93
	140	16.11	12.13	9.53
	160	16.96	12.81	10.10
	180	17.72	13.42	10.63
	200	18.30	13.90	11.03
21	20	4.39	3.05	2.23
	40	8.89	6.22	4.57
	60	12.29	8.62	6.34
	80	14.54	10.22	7.54
	100	16.25	11.45	8.45
	120	17.47	12.33	9.11
	140	18.60	13.16	9.74
	160	19.66	13.93	10.33
	180	20.62	14.65	10.88
	200	21.36	15.22	11.31
41	20	4.56	3.09	2.24
	40	9.33	6.32	4.58
	60	12.92	8.77	6.36
	80	15.31	10.40	7.55
	100	17.14	11.65	8.47
	120	18.45	12.55	9.13
	140	19.69	13.41	9.75
	160	20.86	14.22	10.35
	180	21.94	14.97	10.90
	200	22.79	15.56	11.34

The incident electron energies are $E_0 = 100$ keV, $E_0 = 200$ keV, $E_0 = 500$ keV. The collection angles range from $\beta = 1$ to $\beta = 41$ mrad and values for the energy window are from $\Delta = 20$ to $\Delta 200$ eV.

Table 2
Values of the Mo M_{45} cross sections given by our calculations

β (mrad)	Δ (eV)	$E_0 = 100$ keV σ (barns)	$E_0 = 200$ keV σ (barns)	$E_0 = 500$ keV σ (barns)
1	20	0.19×10^3	0.31×10^3	0.48×10^3
	40	0.50	0.82	1.33
	60	0.90	1.49	2.48
	80	1.31	2.23	3.79
	100	1.69	2.91	5.05
	120	2.01	3.50	6.18
	140	2.29	4.01	7.21
	160	2.52	4.46	8.14
	180	2.72	4.85	8.98
	200	2.89	5.18	9.70
6	20	1.29	1.15	1.11
	40	3.60	3.26	3.17
	60	6.62	5.99	2.48
	80	10.05	9.12	8.64
	100	13.36	12.19	11.56
	120	16.37	15.01	14.28
	140	19.10	17.61	16.82
	160	21.59	20.02	19.20
	180	23.83	22.21	21.39
	200	25.77	24.14	23.33
11	20	1.81	1.52	1.41
	40	5.17	4.34	3.99
	60	9.32	7.71	6.81
	80	14.06	11.56	10.02
	100	18.71	15.39	13.28
	120	23.00	18.97	16.36
	140	26.96	22.30	19.26
	160	39.12	25.41	21.98
	180	43.49	28.26	24.50
	200	36.86	30.79	26.76
21	20	2.51	2.02	1.68
	40	7.13	5.70	4.78
	60	12.23	9.49	7.81
	80	18.01	13.78	11.14
	100	23.84	18.15	14.55
	120	29.28	22.27	17.80
	140	34.37	26.16	20.87
	160	39.12	29.81	23.78
	180	43.49	33.19	26.48
	200	47.36	36.20	28.90
41	20	3.34	2.41	1.75
	40	9.43	6.86	5.02
	60	15.14	10.96	8.11
	80	21.42	15.41	11.47
	100	27.87	19.98	14.92
	120	33.98	24.33	18.20
	140	39.77	28.46	21.33
	160	45.21	32.36	24.28
	180	50.26	35.98	27.03
	200	54.75	39.22	29.48

The incident electron energies are $E_0 = 100$ keV, $E_0 = 200$ keV, $E_0 = 500$ keV. The collection angles range from $\beta = 1$ to $\beta = 41$ mrad and values for the energy window are from $\Delta = 20$ to $\Delta = 200$ eV.

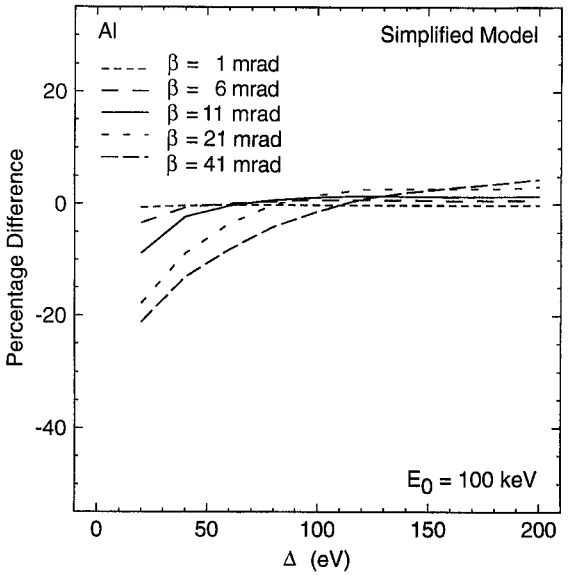

Fig. 3. The percentage difference of the simplified model (Section 3) compared to the more fundamental model (Section 2) versus energy collection window Δ for Al L_{23} excitations. The incident electron energy is 100 keV. Values of the collection angle β vary from 1 to 41 mrad.

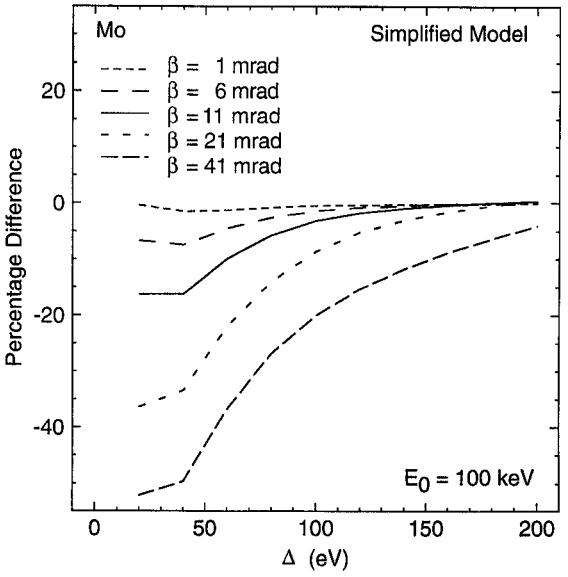

Fig. 4. Same as Fig. 3, but for Mo M_{45} excitations.

values of β between 1–41 mrad. It is found that the percentage difference between σ and σ_A decreases with increasing Δ and decreasing values of β.

The cross sections, σ and σ_A, calculated in this work are expected to be most accurate for small values of β because this condition implies small values of momentum transfer. For $\beta = 1$ mrad and the energies considered here, $E_0 = 100$–500 keV, the maximum momentum transfer q_{max} given by Eq. (15c) is such that $q_{max}a_0$ takes values 0.1 to 0.4; consequently, $\epsilon_2^{nl}(q_{max}, \omega) \simeq \epsilon_2^{nl}(q = 0, \omega)$ to within a few percent according to our calculations. The use of a normalization factor, Eq. (9), ensures that in this case the cross section is determined entirely by the experimental data $\epsilon_2^{EXP}(\omega)$ rather than from the calculated values, ϵ_2^{nl}. Consequently, the present calculation is expected to be very accurate for $\beta = 1$ mrad.

We compare our results with other calculations: the constant-oscillator-strength model, the Rez model, and Egerton's computer program (SIGMAL3). The constant-oscillator-strength model assumes that the matrix element in Eq. (7) is constant. Because of the use of experimental optical data, as discussed in the previous paragraph, this model will also be most accurate for small values of β. The Rez model [13] is modified by us so that it makes use of optical data in the same way as for our work. This procedure ensures that it also gives correct values for the cross sections for small values of β. Egerton's computer program is based on a hydrogenic model with an empirical correction based on photoabsorption data.

Plots of the percentage difference between the constant-oscillator-strength model and our calculations as a function of the energy collection window are shown in Figs. 5 and 6 for Al and Mo, respectively, for an incident electron energy of 100 keV and values of β between 1 and 41 mrad. Similar plots of the percentage difference between the Rez model and our model are shown in Figs. 7 and 8 for Al and Mo. Figs. 5 and 7 for Al and Figs. 6 and 8 for Mo are quite similar. This result occurs because the Rez model predicts the matrix element in Eq. (7) to have a weak momentum dependence while the constant-oscillator-strength model assumes zero momentum dependence. The momentum dependence in our model is quite different, especially for Mo.

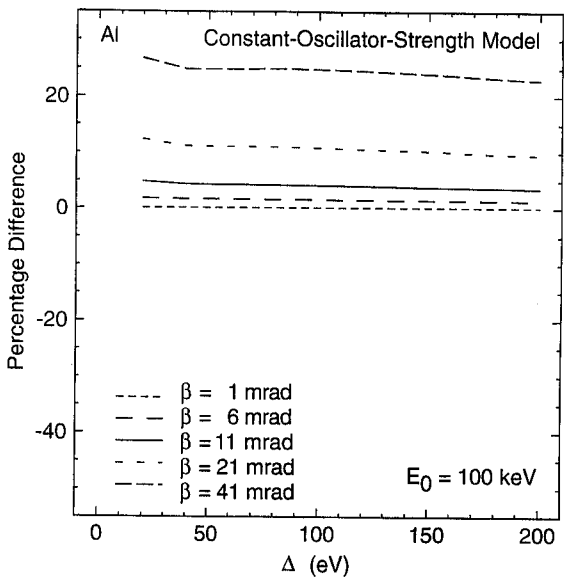

Fig. 5. The percentage difference of the constant-oscillator-strength model compared to our fundamental approach versus energy collection window Δ for Al L_{23} excitations. The incident electron energy is 100 keV. Values of the collection angle β vary from 1 to 41 mrad.

Finally, Egerton has devised a simple calculation for the cross section based on the hydrogenic model that makes use of photoabsorption data. The cross sections are given by his Fortran program [7], and the percentage difference between results from his model and ours is shown in Fig. 9 for Al, an incident electron energy of 100 keV and values of β between 1 and 41 mrad. Even for $\beta = 1$ mrad, where our results are expected to be very accurate, there is a very large discrepancy between the two calculations. As expected, the differences are found to be large for small values of Δ due to the limitations of the hydrogenic model in describing the shape of ϵ_2 near the excitation threshold.

Luo and Zeitler [8] have calculated the M_{45}-shell cross section of Mo using a hydrogenic model for the momentum dependence of $\mathrm{Im}(-1/\epsilon)$. For $E_0 = 60$ keV, $\beta = 10$ mrad, and $\Delta = 100$ eV, they obtain $\sigma = 23.8$ kbarns whereas the present calculation with optical data from Ref. [23] yields

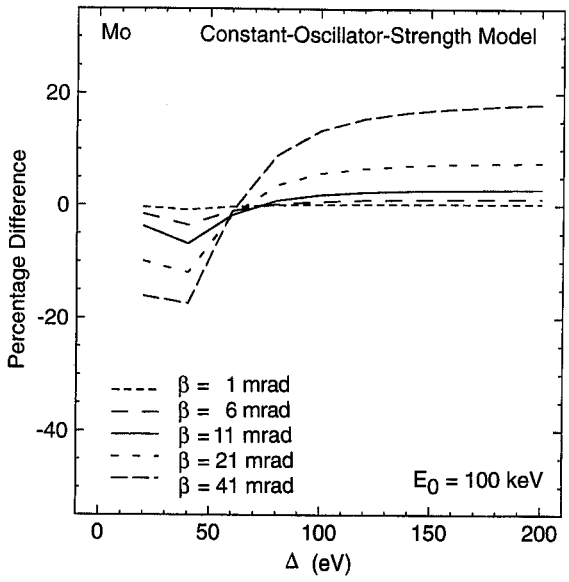

Fig. 6. Same as Fig. 5, but for Mo M_{45} excitations.

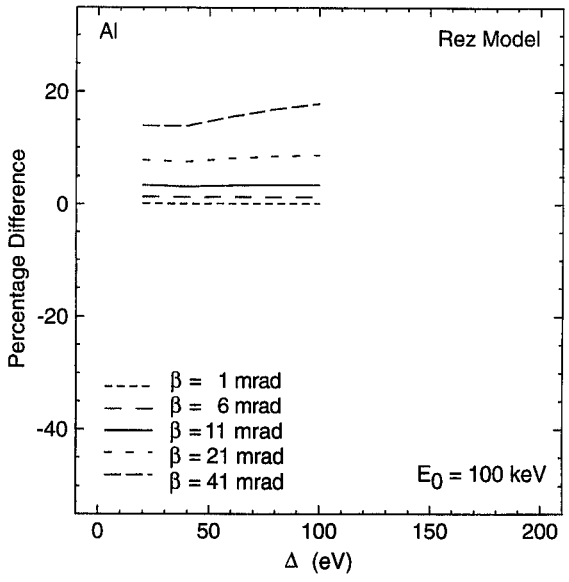

Fig. 7. The percentage difference of the Rez model compared to our fundamental approach versus energy collection window Δ for Al L_{23} excitations. The incident electron energy is 100 keV. Values of the collection angle β vary from 1 to 41 mrad.

$\sigma = 20.0$ kbarn, a difference of about 16%. The calculation of Luo and Zeitler also makes use of similar optical data for describing the dependence of the differential cross-section on energy loss.

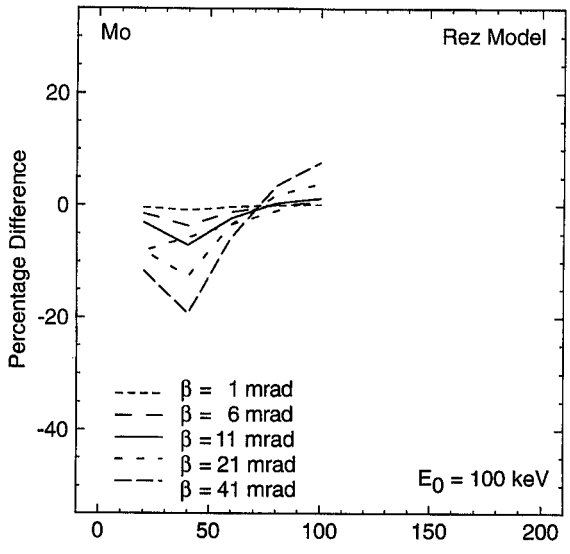

Fig. 8. Same as Fig. 7, but for Mo M_{45} excitations.

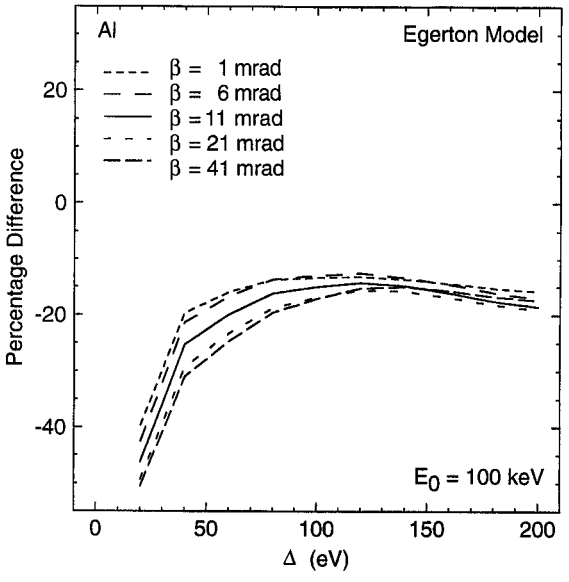

Fig. 9. The percentage difference of the Egerton hydrogenic model compared to our fundamental approach versus energy collection window Δ for Al L_{23} excitations. The incident electron energy is 100 keV. Values of the collection angle β vary from 1 to 41 mrad.

It is clear that very different results for the cross sections are obtained from the various models. This is due to the differing momentum dependences in the models for the matrix element of Eq. (7).

Table 3
Comparison of experimental measurements of Al L_{23} cross sections with our theoretical calculations. The experimental data are from Crozier [20] (C); Hofer et al. [21] (H), and Malis and Titchmarsh [22] (MT) for $E_0 = 100$ keV, $\Delta = 60$ eV, and various values of β

β (mrad)	Experimental cross sections (kbarns)			Theoretical cross sections (kbarns)
	C	H	MT	
5	100 ± 5	63	98	83
21	150 ± 15			123
120	190 ± 30	109		131

For $\beta = 1$ mrad, the matrix element is constant, independent of momentum and all the calculations give essentially identical results (with the exception of Egerton's which does not incorporate optical data in the same way as the other calculations).

In Table 3, cross sections calculated with the present model (Section 2) are compared with experimental results [19–21] for Al L_{23} excitations and the results are in reasonable agreement (although we have assumed the momentum dependence of $\mathrm{Im}(-1/\epsilon)$ to be the same for the Al L_1 core level as for the Al L_{23} levels).

5. Conclusions

We have presented a new model for calculating cross sections for excitations of core electrons by fast electrons. It is assumed that the core electrons are excited to states appropriate to a conduction band in a solid rather than to an atomic state [2–14]. The band state is described by an orthogonalized plane wave with free-electron dispersion. The model makes use of experimental optical data to ensure that the calculated cross sections are correct at small scattering angles. Thus, it is the momentum dependence of the cross section that is modeled as opposed to the dependence on the energy loss. The details of the model have been described in Section 2. The cross sections predicted by the model are shown in Figs. 1 and 2 for Al and Mo, respectively, and numerical values are given in Tables 1 and 2.

We have also introduced a much simpler and more convenient model for the calculation of cross sections. This model, discussed in Section 3, is one that has been used successfully to calculate inelastic mean free paths of fast electrons where conduction band excitations are responsible for most of the inelastic scattering [17, 18]. Although there is no a priori reason for this approach to work well for calculating cross sections involving core excitations, we have carried out such calculations in the hope that they would be in reasonable agreement with our more realistic model. Cross sections for our more accurate model and the simplified model are compared in Figs. 3 and 4 for Al and Mo. For small values of β, the two methods agree very well because they both make use of optical data that ensures correct results for $\beta = 0$. They also agree well if Δ is sufficiently large (i.e., the condition for which inelastic mean free paths were calculated [17, 18]).

We have compared our calculated cross sections with those given by the simpler method discussed above, as well as with cross sections given by three other models. The three other models are (a) the constant-oscillator-strength model, in which the matrix element in Eq. (7) is taken to be constant, (b) the Rez model, an atomic model for the excitations, and where we have normalized the calculated cross section using experimental optical data, and (c) Egerton's hydrogenic model in which he has made use of some experimental optical data. For all the models considered here except Egerton's, the use of optical data guarantees that they yield correct cross sections at small values of the collection angle, β, and that the differences in predicted cross section arise from the momentum dependence, q, of the model.

Results for the different models are compared in Figs. 3–9 for an incident electron energy of 100 keV, values of β from 1 to 41 mrad, and values of the energy collection window from 20–200 eV. Our simplified model gives cross sections that are similar to those given by our more accurate model when the energy collection window is relatively large (greater than 100 eV). The constant-oscillator-strength model gives cross sections that differ from our model by slightly larger amounts than those predicted by the Rez model. In all cases, the

dependence of cross section on energy collection window is very different in Al and Mo due to the differences in the momentum dependence of the generalized oscillator strengths.

The results from our accurate model for Al L_{23} excitations have been compared to results from the Egerton model [7] in Fig. 9, and it can be seen that there are large differences in the predicted cross sections, even for small values of β where our model must give accurate cross sections. Cross sections calculated with the present model have been compared with experimental results [19–21] for Al L_{23} excitations and the results are in reasonable agreement.

Appendix A.

We derive Eqs. (19a), (19b), (19c) and (19d) in the text. The orthogonalized plane wave, ϕ_k, that describes a valence state is given by

$$\phi_k(\boldsymbol{r}) = e^{i\boldsymbol{k}\cdot\boldsymbol{r}} - \sum_{n'l'm'} \langle \phi_{n'l'm'} | e^{i\boldsymbol{k}\cdot\boldsymbol{r}} \rangle \phi_{n'l'm'}(\boldsymbol{r}) \tag{A.1}$$

where the normalization of ϕ_k is neglected because the expression of σ_{nl} given by Eq. (14) involves $\epsilon_2^{nl}(q,\omega)/\epsilon_2^{nl}(q=0,\omega)$ so that the normalization factors approximately cancel. The core wave function is

$$\phi_{nlm}(\boldsymbol{r}) = R_{nl}(r) Y_{lm}(\hat{\Omega}_r) \tag{A.2}$$

and use of

$$e^{i\boldsymbol{k}\cdot\boldsymbol{r}} = 4\pi \sum_{l=0}^{\infty} i^l j^l(kr) \sum_{m=-l}^{l} Y^*_{lm}(\hat{\Omega}_r) Y_{lm}(\hat{\Omega}_k) \tag{A.3}$$

in $\langle \phi_{n'l'm'} | e^{i\boldsymbol{k}\cdot\boldsymbol{r}} \rangle$ yields

$$\langle \phi_{n'l'm'} | e^{i\boldsymbol{k}\cdot\boldsymbol{r}} \rangle = 4\pi i^{l'} Y^*_{l'm'}(\hat{\Omega}_k) u_{n'l'}(k), \tag{A.4a}$$

where

$$u_{n'l'}(k) = \int_0^{\infty} dr\, r^2 j_{l'}(kr) R_{n'l'}(r). \tag{A.4b}$$

The wave function ϕ_k then takes the form

$$\phi_k(\boldsymbol{r}) = \frac{e^{i\boldsymbol{k}\cdot\boldsymbol{r}}}{V^{1/2}} - \frac{4\pi}{V^{1/2}} \sum_{n'l'm'} i^{l'} Y^*_{l'm'}(\hat{\Omega}_k) u_{n'l'}(k) \phi_{n'l'm'}(\boldsymbol{r}). \tag{A.5}$$

Use of Eq. (A.4a) in

$$M_{nlm}(k,q) = \langle \phi_k | e^{-i\boldsymbol{q}\cdot\boldsymbol{r}} | \phi_{nlm} \rangle$$

yields

$$M_{nlm} = M^{(1)}_{nlm} + M^{(2)}_{nlm}, \tag{A.6a}$$

where

$$M^{(1)}_{nlm} = \left\langle \frac{e^{i\boldsymbol{k}\cdot\boldsymbol{r}}}{V^{1/2}} | e^{-i\boldsymbol{q}\cdot\boldsymbol{r}} | \phi_{nlm} \right\rangle \tag{A.6b}$$

$$M^{(2)}_{nlm} = -\frac{4\pi}{V^{1/2}} \sum_{n'l'm'} (-i)^{l'} Y_{l'm'}(\hat{\Omega}_k)\, u^*_{n'l'}(k) \times \langle \phi_{n'l'm'} | e^{-i\boldsymbol{q}\cdot\boldsymbol{r}} | \phi_{nlm} \rangle. \tag{A.6c}$$

Expanding $e^{i\boldsymbol{q}\cdot\boldsymbol{r}}$ and $e^{i\boldsymbol{k}\cdot\boldsymbol{r}}$ via Eq. (A.3) and substituting the result in Eq. (A.6b) gives

$$M^{(1)}_{nlm} = \frac{(4\pi)^2}{V^{1/2}} \sum_{l'l''m'm''} \Gamma_{nll'l''}(k,q) W(l'm'l''m''lm)(-i)^{l'+l''} \times Y_{l'm'}(\hat{\Omega}_k) Y^*_{l''m''}(\hat{\Omega}_k), \tag{A.7a}$$

where Γ is given by Eq. (19d) and

$$W(l'm',l''m'',lm) = \int d\hat{\Omega} Y^*_{l'm'}(\hat{\Omega}) Y_{l''m''}(\hat{\Omega}) Y_{lm}(\hat{\Omega}) \tag{A.7b}$$

$$= (l' \| Y_{l''} \| l)(-1)^{l'-m'} \begin{pmatrix} l' & l'' & l \\ -m' & m'' & m \end{pmatrix}, \tag{A.7c}$$

where

$$(l' \| Y_{l''} \| l) = (-1)^{l'} [(2l'+1)(2l''+1)(2l+1)]^{1/2} \times (4\pi)^{-1} \begin{pmatrix} l' & l'' & l \\ 0 & 0 & 0 \end{pmatrix} \tag{A.7d}$$

and

$$\begin{pmatrix} l' & l'' & l \\ -m' & m'' & m \end{pmatrix}$$

is a $3-j$ symbol.

Expanding $e^{-i\boldsymbol{q}\cdot\boldsymbol{r}}$ as in Eq. (A.3) and substituting in Eq. (A.6c) gives

$$M^{(2)}_{nlm} = \frac{-(4\pi)}{V^{1/2}} \sum_{n'l'l''m'm''} (-1)^{l'+l''} u_{n'l'}(k) \theta_{nn'll'l'}(q) W \times (l'm',l''m'',lm) Y_{l'm'}(\hat{\Omega}_k) Y^*_{l''m''}(\hat{\Omega}_q), \tag{A.8}$$

where $\theta_{nn'll'l''}$ is defined in Eq. (19c).

The quantity $|m_{nl}(k,q)|^2$ defined in Eq. (12) is required for evaluating the cross section. From Eq. (12) and (A.6a)

$$|m_{nl}(k,q)|^2 = |m_{nl}^{(1)}(k,q)|^2 + |m_{nl}^{(2)}(k,q)|^2 + c_{nl}(k,q) \tag{A.9a}$$

where

$$|m_{nl}^{(i)}(k,q)|^2 = \int d\hat{\Omega}_k \sum_m |M_{nlm}^{(i)}(k,q)|^2, \quad i = 1,2 \tag{A.9b}$$

and

$$c_{nl}(k,q) = \int d\hat{\Omega}_k M_{nlm}^{(1)*}(k,q) M_{nlm}^{(2)}(k,q) + \text{c.c.} \tag{A.9c}$$

where c.c. denotes the complex conjugate of the previous term.

Use of Eqs. (A.7a) and (A.8) in Eqs. (A.9a), (A.9b) and (A.9c) yields

$$|m_{nl}^{(1)}(k,q)|^2 = \frac{(4\pi)^3}{V} \sum_{l'l''} \Gamma_{nll'l''}^2(k,q)(l' \| Y_{l''} \| l)^2 \tag{A.10a}$$

$$|m_{nl}^{(2)}(k,q)|^2 = \frac{(4\pi)^2}{V} \sum_{n'n''l'l''} u_{n'l'}(k) u_{n''l''}(k) \theta_{nn'll'l''}(q) \times \theta_{nn''ll'l''}(q) \times (2l+1)(2l'+1)(2l''+1) \begin{pmatrix} l' & l'' & l \\ 0 & 0 & 0 \end{pmatrix} \tag{A.10b}$$

$$c_{nl}(k,q) = -2\frac{(4\pi)^2}{V} \sum_{n'l'l''} \Gamma_{nll'l''}(k,q) u_{n'l'}(k) \theta_{nn'll'l''}(q) \times (2l+1)(2l'+1)(2l''+1) \begin{pmatrix} l' & l'' & l \\ 0 & 0 & 0 \end{pmatrix}, \tag{A.10c}$$

where u, θ, Γ, are defined in Eqs. (19b), (19c) and (19d). In deriving Eqs. (A.10a), (A.10b) and (A.10c), use has been made of

$$\int d\hat{\Omega}_k Y_{l'm'}^*(\Omega_k) Y_{lm}(\hat{\Omega}_k) = \delta_{l,l'} \delta_{m,m'} \tag{A.11}$$

and

$$\sum_{mm'} \begin{pmatrix} l' & l'' & l \\ -m' & m'' & m \end{pmatrix} \begin{pmatrix} l' & l^{iv} & l \\ -m' & m^{iv} & m \end{pmatrix} = \delta_{l'',l^{iv}} \delta_{m'',m^{iv}} / (2l''+1) \tag{A.12}$$

Because of the infinite summations over $l'l''$ in Eq. (A.10a), it is more useful to evaluate $|m_{nl}^{(1)}(k,q)|^2$ by expanding $e^{-i(q+k)\cdot r}$ in the term $\langle e^{ik\cdot r}|e^{-iq\cdot r}|\phi_{nlm}\rangle$ as

$$e^{-i(q+k)\cdot r} = \sum_{l=0}^{\infty} i^l j_l(|k+q|r) 4\pi \sum_{m=-l}^{l} Y_{lm}^*(\hat{\Omega}_r) Y_{lm}(\hat{\Omega}_{k+q})$$

rather than expanding $e^{-iq\cdot r}$ and $e^{-ik\cdot r}$ separately. The result is the last term in Eq. (19a).

Appendix B.

The expression for $|m_{nl}(k,q\to 0)|^2$ given by Eqs. (20a) and (20b) is derived. Eq. (10) gives

$$m_{nlm}(k,q\to 0) = -iq \cdot \langle \phi_k | \boldsymbol{r} | \phi_{nlm} \rangle \tag{B.1}$$

where ϕ_k is given by Eq. (A.1). Because $|m_{nl}(k,q)|^2$ given by Eq. (12) involves an average over $\hat{\Omega}_k$ it is independent of the direction of q and it is assumed $\boldsymbol{q}$ is in the z directions so that

$$M_{nlm}(k,q\to 0) = -iq\langle \phi_k | z | \phi_{nlm} \rangle \tag{B.2a}$$

$$= -iq(M^{(1)} + M^{(2)}), \tag{B.2b}$$

where

$$M^{(1)} = \left\langle \frac{e^{ik\cdot r}}{V^{1/2}} | z | \phi_{nlm} \right\rangle, \tag{B.2c}$$

$$M^{(2)} = -\sum_{n'l'm'} \left\langle \phi_{n'l'm'} | \frac{e^{ik\cdot r}}{V^{1/2}} \right\rangle^* \langle \phi_{n'l'm'} | z | \phi_{nlm} \rangle. \tag{B.2d}$$

Use of Eq. (A.3) for $e^{ik\cdot r}$ in Eq. (B.2c) yields

$$M^{(1)} = \left[\sum_{l'} \frac{4\pi}{V^{1/2}} (-i)^{l'} T_{l',nl}(k) \right] \Phi_{l'lm} Y_{l'm}(\hat{\Omega}_k), \tag{B.3a}$$

where

$$T_{l',nl}(k) = \int dr\, r^3 j_{l'}(kr) R_{nl}(r), \tag{B.3b}$$

$$\Phi_{l'lm} = \int d\hat{\Omega} Y_{l'm}^*(\hat{\Omega}) Y_{lm}(\hat{\Omega}) \cos\theta. \tag{B.3c}$$

Use of Eq. (A.3) in Eq. (B.2d) yields

$$M^{(2)} = -\left[\frac{4\pi}{V^{1/2}} \sum_{l'} (-i)^{l'} \sum_{n'} u_{n'l'}(k) S_{n'l',nl} \right] \Phi_{l'lm} Y_{l'm}(\hat{\Omega}_k), \tag{B.4a}$$

where $u_{n'l'}(k)$ is defined in Eq. (19b) and

$$S_{n'l',nl} = \int dr\, r^3 R_{n'l'}(r) R_{nl}(r) \tag{B.4b}$$

and $\Phi_{l',lm}$ is given by Eq. (B.3c). The quantity $\Phi_{l',lm}$ is non-zero only for $l' = l \pm 1$,

$$\Phi_{l+1,lm} = [(l+1)^2 - m^2]^{1/2}/[(2l+1)(2l+3)]^{1/2}, \tag{B.5a}$$

$$\Phi_{l-1,lm} = [l^2 - m^2]^{1/2}/[(2l-1)(2l+1)]^{1/2}. \tag{B.5b}$$

Integrating $|M_{nlm}(k,q \to 0)|^2$ over $\hat{\Omega}_k$ gives

$$\int d\hat{\Omega}_k |M_{nlm}(k,q \to 0)|^2 = \frac{(4\pi)^2}{V} q^2 \left[A^2_{l+1,nl}(k)\Phi^2_{l+1,lm} + A^2_{l-1,nl}(k)\Phi^2_{l-1,lm} \right], \tag{B.6a}$$

where

$$A_{l\pm1,nl}(k) = T_{l\pm1,nl} - \sum_{n'} u_{n'l\pm1} S_{n'l\pm1,nl}. \tag{B.6b}$$

Finally,

$$|m_{n,l}(k,q \to 0)|^2 = \sum_m \int d\hat{\Omega}_k |M_{nlm}(k,q \to 0)|^2 = (4\pi)^2 q^2 \left[\frac{(l+1)}{3} \frac{(2l+1)}{(2l+3)} A_{l+1,nl}(k) + \frac{l}{3} A^2_{l-1,nl}(k) \right]. \tag{B.7a}$$

References

[1] R.F. Egerton, Microsc. Micronal. Microstruct. 2 (1991) 203.
[2] M. Inokuti, Rev. Mod. Phys. 43 (1971) 297.
[3] M.C. Walske, Phys. Rev. 101 (1956) 940.
[4] B.H. Choi, Phys. Rev. A 7 (1973) 2056.
[5] B.H. Choi, E. Merzbacher, G.S. Khandelwal, At. Data 5 (1973) 291.
[6] R.F. Egerton, Ultramicroscopy 4 (1979) 169.
[7] R.F. Egerton, Electron Energy-Loss Spectroscopy in the Electron Microscope, 2nd ed., Plenum, NY, 1996.
[8] B.P. Luo, E. Zeitler, J. Electron Spect. and Related Phenomena 57 (1991) 285.
[9] E.H. McGuire, Phys. Rev. A 3 (1971) 267.
[10] S.T. Manson, Phys. Rev. A 6 (1972) 135.
[11] J.H. Scofield, Phys. Rev. A 18 (1978) 963.
[12] R.D. Leapman, P. Rez, D.F. Mayers, J. Chem. Phys. 72 (1980) 1232.
[13] P. Rez, Ultramicroscopy 9 (1982) 283.
[14] C.C. Ahn, P. Rez, Ultramicroscopy 17 (1985) 105.
[15] J. Hubbard, Proc. Phys. Soc. A 68 (1955) 976.
[16] E. Clementi, C. Roetti, At. Data Nuc. Data Tables 14 (3–4) (1974) 177.
[17] D.R. Penn, Phys. Rev. B 35 (1987) 482.
[18] S. Tanuma, C.J. Powell, D.R. Penn, Surf. Interface Anal. 21 (1994) 165.
[19] D. Smith, E. Shiles, M. Inokuti, in: E. Palik (Ed.), Handbook of Optical Constants of Solids, Academic Press, New York, 1985, p. 369.
[20] P.A. Crozier, Phil. Mag. B 61 (1990) 311.
[21] F. Hofer, P. Golob, A. Bruneggar, Ultramicroscopy 25 (1988) 81.
[22] T. Malis, J.M. Titchmarsh, in: G.J. Tatlock (Ed.), Electron Microscopy and Analysis, Inst. Phys. Conf. Ser. 78 (1985) 181.
[23] D.W. Lynch, W.R. Hunter, in: E. Palik (Ed.), Handbook of Optical Constants of Solids, Academic Press, NY, 1985, p. 303.